Computer Methods and Programs in Biomedicine 221 (2022) 106896

Contents lists available at ScienceDirect

Computer Methods and Programs in Biomedicine

journal homepage: www.elsevier.com/locate/cmpb

Experimental and computational model approach to assess the photothermal effects in transparent nanocrystalline yttria stabilized zirconia cranial implant

Mildred S. Cano-Velázquez[a], Jose Bon[b], M. Llamazares[c], Santiago Camacho-López[d], Guillermo Aguilar[e], Juan Hernández-Cordero[a], Macarena Trujillo[c,*]

[a] Instituto de Investigaciones en Materiales, Universidad Nacional Autónoma de México, Ciudad de México, México
[b] Food Technology Department, Universitat Politècnica de València, Valencia, Spain
[c] Department of Applied Mathematics, BioMIT, Universitat Politècnica de València, Valencia, Spain
[d] Centro de Investigación Científica y de Educación Superior de Ensenada (CICESE), Ensenada, B.C., México
[e] J. Mike Walker '66 Department of Mechanical Engineering, Texas A&M University, College Station, TX, USA

ARTICLE INFO

Article history:
Received 1 September 2021
Revised 12 May 2022
Accepted 15 May 2022

Keywords:
Nanocrystalline yttria stabilized zirconia
Cranial implant
Heat conduction
Window to the brain
Computer modeling
Photothermal effect

ABSTRACT

Background and objective: In the last few years, we have been exploring the use of transparent nanocrystalline yttria-stabilized zirconia (nc-YSZ) ceramics as a biomedical transparent cranial implant, referred as the "Window to the Brain" (WttB). The WttB aims at providing chronical optical access to the brain for diagnostics and therapeutic procedures and it has shown to provide an effective means to obtain enhanced results from optical imaging techniques. The objective of this work is to explore the photothermal effects of the Wttb produced when it is irradiated by a laser source.

Methods: We make experimental and computer models. The thermal effects of laser irradiation on the nc-YSZ samples were evaluated upon registering the induced temperature changes by means of thermal imaging. The computer models try to mimic the experimental models using a similar geometry, reproducing the physical situation by a couple thermal-optical problem and adjusting the main parameters from the experimental results.

Results: Experimental and computational coincides in results: Temperatures at the bottom surface of the implant does not exceed those which produce thermal damage. The quantitative comparison between experimental and computational models show that differences in results are under a reasonable value of 5% and qualitatively we observe a similar behavior. The results provide optimum values for the thermal-optical nc-YSZ parameters considering a linear and exponential relationship with temperature for the absorption coefficient: The thermal conductivity is $k = 2.13$ W/m·K and the absorption coefficient α varies from 426 to 526 m^{-1} with the linear relationship, and $k = 2.04$ W/m·K and $\alpha \in [433,502]$ m^{-1} with the exponential. The reflection coefficient is $R = 19\%$ in both cases.

Conclusions: The temperatures achieved in the nc-YSZ during the laser irradiation are suitable for biomedical applications. The combination of experimental and computational models contributes to build a clinically oriented model with the thermal-optical parameters values stablished and to determine their influence in results. Specifically, the absorption coefficient of the nc-YSZ samples is the most influent parameter in the obtained temperatures. Moreover, this combination provides a method to evaluate the relevant thermal-optical parameters of nc-YSZ samples obtained with different manufacturing processes.

1. Introduction

Polycrystalline zirconia-based ceramics have become the focus of recent investigations because of their unique combination of properties. Their high hardness and chemical inertness (high temperature stability and corrosion resistance) make them important target materials for various applications [1,2]. Well-proven

* Corresponding author.
E-mail address: matrugui@mat.upv.es (M. Trujillo).

https://doi.org/10.1016/j.cmpb.2022.106896

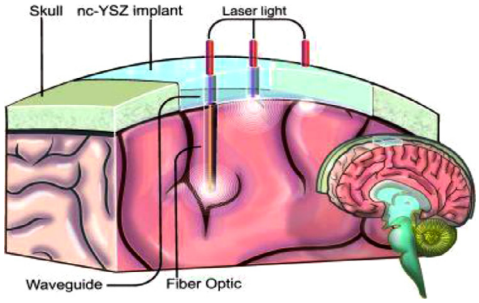

Fig. 1. Conceptual scheme of the "Windows to the Brain" (WttB) platform.

biocompatibility, low thermal conductivity, and high oxygen diffusivity have made zirconia-based ceramics a favorable option for biomedical applications [3–7]. Furthermore, by decreasing the grain size of the polycrystalline ceramics to the nanoscale, novel characteristics such as high density (low porosity), transparency/translucency, high refractive index and Abbe number have been reported [8–10]. The advent of zirconia-based ceramics with tailored crystallinity at the nano-scale, combining hardness, biocompatibility and optical transparency will certainly foster novel developments in biomedical-related applications.

In the last few years, we have been exploring the use of transparent nanocrystalline yttria-stabilized zirconia (nc-YSZ) ceramics as a biomedical transparent cranial implant, referred to in the literature as the "Window to the Brain" (WttB) implant [11]. The concept of the WttB shown schematically in Fig. 1, aims at providing chronical optical access to the brain for diagnostics and therapeutic procedures [12,13]; thus far, it has shown to offer an effective means to obtain enhanced results from optical imaging techniques [14–17] and further promises to extended the reach of ultrasound-based therapies [18]. The transparency of the nc-YSZ is achieved by using ultra-fine yttria-stabilized zirconia (YSZ) powder and a ceramic processing method known as current-activated pressure-assisted densification (CAPAD) yielding a highly transparent material in the spectral range of interest for medical imaging and laser therapies of the brain tissue [16–19]. For some spectral ranges however, the nc-YSZ shows absorption and scattering features that can lead to a local increase in temperature of the material. Remarkably, this photothermal effect has also shown excellent potential for laser assisted biomedical procedures; as an example, it has been demonstrated as a means to conduct bacterial anti-fouling through the WttB implant [20]. Other therapeutic practices such as thermal therapy for cancer treatment may also benefit from these photothermal effects [21], and this is particularly attractive for brain tumors given their intricated accessibility [22]. Evidently, the effectiveness of these thermally-driven procedures rely on the temperature ranges that can be achieved through laser irradiation, and hence the photothermal effects in the nc-YSZ are extremely relevant.

Although the optical and thermal characteristics of nc-YSZ have been reported previously [19,23], the photothermal effects in this material and the value of some parameters have not been fully explored. Our objective in this paper is to provide a better insight of the photothermal effects produced in the nc-YSZ implant when irradiated by a laser source and thus obtain guidelines for their potential use in biomedical procedures. Albeit based on relatively simple experimental and computational models, our analysis of the photothermal behavior of the material used for the WttB implants provides a computational tool that may serve as a means to evaluate its performance in more complicated scenarios. Specifically, our interest is (1) to study the thermal behavior of the nc-YSZ samples and (2) to determine the main features of the material involved in the photothermal effects. In this sense, we use an experimental approach for (1) and a computer model for (2). Experimentally we assess the increase in temperature in the laser irradiated regions of the samples through thermal imaging. These results are then used for adjusting the parameters of the computer model in order to obtain temperatures that will closely match the experimental temperatures. As shown in our results, this approach renders an effective means to reproduce with the computer model the photothermal effects observed experimentally in the nc-YSZ under different conditions for laser irradiation. Hence, the computer model effectively allows for assessing the influence of the optical and thermal parameters of the nc-YSZ samples on the temperature profiles obtained experimentally, thereby providing a useful means to estimate the required laser powers to achieve a target temperature for biomedical thermal procedures through the implant. The computer model is also validated using the temperature data extracted for the previous experiment related in [20].

2. Methods 1: experimental model

Transparent nanocrystalline 8 mol% $YO_{1.5}$ yttria-stabilized zirconia (nc-YSZ) implant samples were produced from a precursor YSZ nanopowder (Tosoh USA, Inc., Grove City, OH, USA) densified into a transparent bulk ceramic using CAPAD as described previously [19]. The samples were disk-shaped with a radius of 19.5 mm and their thickness were reduced from 1 mm to ≈600 μm by polishing with a 30 μm diamond slurry on an automatic polisher (Pace Technologies, Tucson, Arizona USA). The disks were then polished with successively finer diamond and silica slurries ranging from 6 to 0.2 μm yielding a final thickness of 574.5 μm. Samples were sectioned in two semicircles using a diamond lapping saw (DTQ-5, WEIYI, Qingdao, China), followed by sonication in acetone and thorough rinsing in water.

The thermal effects of laser irradiation on the nc-YSZ samples were evaluated upon registering the induced temperature changes by means of thermal imaging. Experiments were carried out using a fiber-coupled 810 nm continuous wave NIR laser (Vari-Lase REF946, Vascular Solutions, Morrisville, NC, USA) to irradiate the implant. As depicted in Fig. 2a, the fiber was coupled to an optogenetics patch-cord cable (M125L01, Thorlabs, Newton, NJ, USA) allowing laser delivery through an interconnector (ADAL3, Thorlabs, Newton, NJ, USA) and a cannula (CFMXD20, Thorlabs, Newton, NJ, USA) directly attached to the implant. The latter was glued to the nc-YSZ samples with dental cement and the resulting irradiation spot was 400 μm. The thermal profile due to laser irradiation was monitored at the opposite surface of the implant using a sequence of thermal images recorded by a non-contact infrared thermal camera (A325sc, FLIR Systems Inc., Wilsonville, OR), operating in video mode at 60 frames/s over the spectral range of 7.5–13 μm. All the experiments were carried out setting the laser output power at 3 W and varying the exposure times upon adjusting the on-off cycles of the laser. For each experimental condition, thermal images were obtained during the on-off cycle of the laser yielding a sequence of images such as that shown in Fig. 2b. These images were subsequently processed to obtain the time evolution of the maximum temperature registered by the camera. Since the beam has a gaussian profile, the maximum temperature achieved was assessed by selecting the data corresponding to the central part of the spot registered in the thermal image (see Fig. 2b).

Because the nc-YSZ is essentially opaque over the wavelength range of the camera (see Ref. [20]), the IR radiation measured by the camera is primarily emitted by the upper surface of the samples. In general, variations with temperature in the emissivity of the surface material must be accounted for when acquiring the temperature readings through thermal imaging. However, for zirconia ceramics, an increase in the emissivity has been shown to occur at temperatures greater than 1400 K [24], which are far above

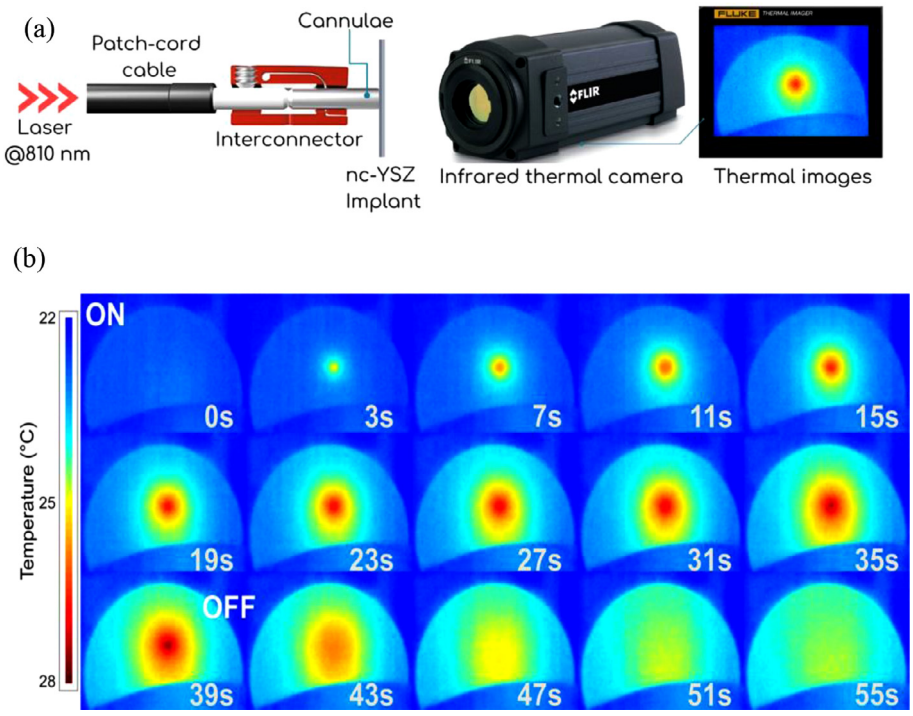

Fig. 2. (a) Experimental setup used for irradiating the nc-YSZ samples and for thermal imaging (see text for further details). (b) Typical sequence of thermal images obtained with the IR camera during laser exposure. The laser was turned on at $t = 0$ s and turned off at $t = 40$ s. An increase in temperature is clearly seen within the irradiated region of the nc-YSZ sample.

from the temperature reached in our experiments. It has further been reported that the emissivity of these ceramics shows a weak temperature dependence from 867 to 1298 K for a spectral range from 1 to 14 μm [24]. Thus, no additional adjustments were made to the temperature readings obtained with the thermal camera.

In order to evaluate the heating and cooling rates of the nc-YSZ, two sets of experiments with different laser irradiation cycles were performed. In Experiment 1 we performed a single cycle with 40 s of exposure time (laser on) and 15 s of cooling time (laser off); the latter was determined to be an adequate time for the temperature to return to its initial value through experimental observations. Experiment 2 was performed upon varying the on-off time intervals of the laser: we first used 4 irradiation cycles with 10 s of laser irradiation and 10 s for cooling, and finally, a single cycle of 10 s with the laser on and a 5 s interval for cooling (i.e., laser off). For all experiments the initial room temperature (T_a) was measured to be within 23 °C.

3. Methods 2: computer models

The model used for assessing the influence of the optical and thermal parameters of the nc-YSZ samples through computer simulations was based on the experimental arrangement described in the previous section. Validation of the model was performed upon replicating the results on bacterial anti-fouling using laser irradiation through the nc-YSZ [20]. As shown in Fig. 3, the experimental arrangements lend itself to some computational simplifications: we first consider that the gaussian profile of the laser yields a temperature profile with axial symmetry and thus the computational domains can be defined as shown in the figure. Next, we consider two domains for the nc-YSZ implant: one defined by the laser irradiated region and one delimited by the geometry of the sample. The irradiated region is delimited by the laser spot (400 μm diameter) and by the thickness of the samples.

The thermal effects in the nc-YSZ samples during laser irradiation were simulated using the heat equation. Thus, the temperature T was obtained upon solving:

$$\rho c \frac{\partial T}{\partial t} = \nabla \cdot (k \nabla T) + Q \tag{1}$$

where ρ is the density, c the specific heat, k is thermal conductivity and Q is the source term representing the heat generated through laser irradiation. This heat generation term was only considered for the section of the sample material exposed to the laser source (Domain 1, marked in red in Fig. 3) and was evaluated as $Q = \alpha I$, where α is the absorption coefficient of the material and I the light intensity. Scattering effects in the samples were considered to be minimum, and I was thus obtained using Beer-Lambert's equation:

$$\frac{\partial I}{\partial z} = \alpha I \tag{2}$$

Aside from the axisymmetric geometrical considerations, null flux conditions were imposed for the rest of the boundaries. Reflection of the laser from the surface of the nc-YSZ was accounted for evaluating the intensity as:

$$I = I_0(1 - R)e^{-r^2} \tag{3}$$

where I_0 is the laser intensity impinging on the sample and R is the reflectivity of the material. Eq. (3) assumes a gaussian intensity distribution of the laser beam around the origin, located at the center of laser spot (see Fig. 3). In this way, the laser load is modeled as a boundary condition of the optical problem, and the solution of this problem will be used as the volume heat source ($Q = \alpha I$) of the thermal problem according to (1). For the thermal conditions, we assumed an initial temperature T_a corresponding to the room temperature registered initially for each experiment. Additionally, natural heat convection was considered for both surfaces of the nc-YSZ samples, although different convection coefficients (h_t and h_b) were used for the laser irradiated side and for

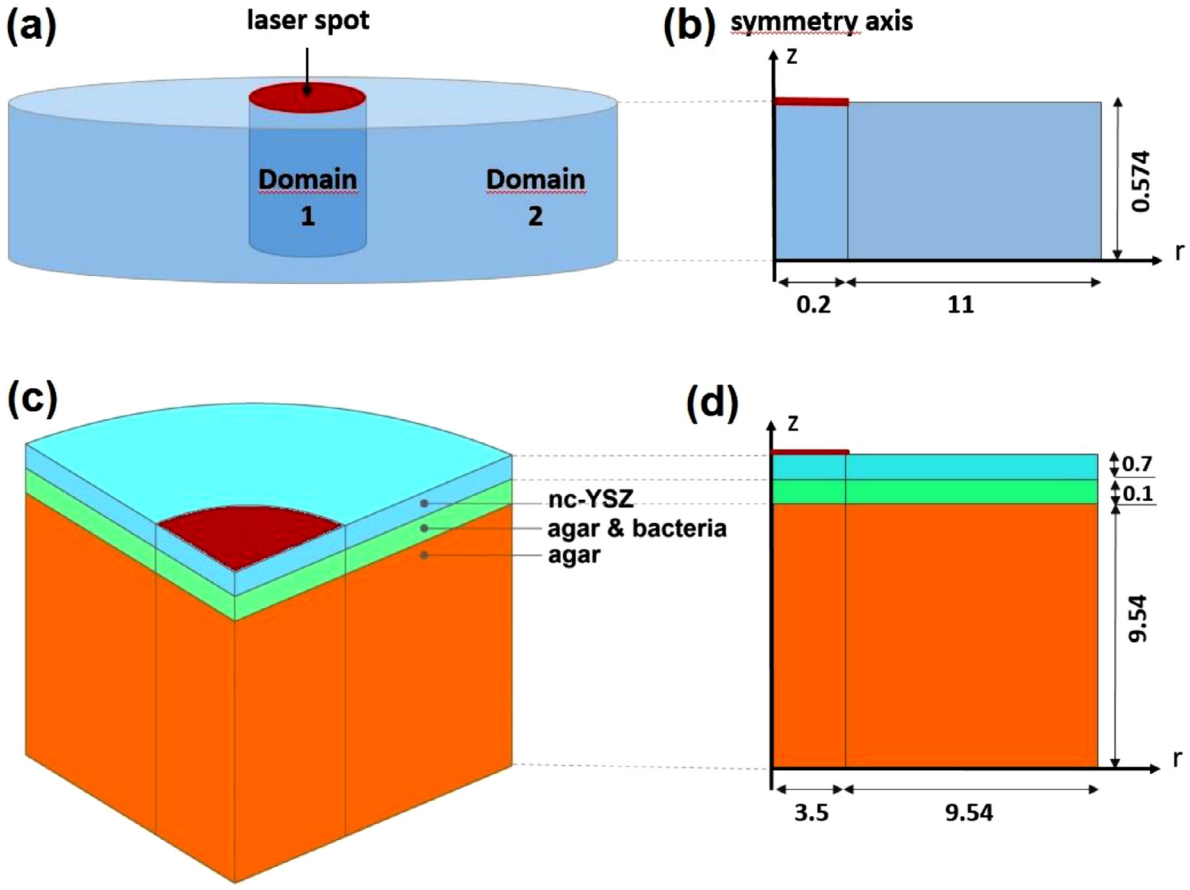

Fig. 3. (a) and (c): 3D schematic representation of the geometry of the experimental arrangement described in Section 2 and for the experiments reported in [20], respectively. (b) and (d) are the 2D-axial symmetrical geometries used for the computational models as a simplification of the 3D geometries shown in (a) and (c), respectively, (dimensions are shown in mm and the schemes out of scale).

the opposite end of the sample. In a previous report [20], natural heat convection was set only at the upper surface of the implant and a constant temperature of 37 °C was set at the bottom. Finally, we considered thermal insulation conditions from the surrounding medium.

3.1. Parameters and optimization

To assess the influence of the ns-YSZ parameters and for estimating their values, the calculations were based on the experimental results obtained with the arrangement described in Section 2. The values for the intensity impinging on the samples (I_0) and the initial temperature (T_a) were obtained from these experiments and the values for the parameters of the nc-YSZ samples, namely the density and specific heat, were taken as $\rho = 6042$ kg/m^3 and c=427 J/kg·K, in accordance to previous reports [20]. However, for the thermal conductivity (k), the absorption coefficient (α) and the reflectivity (R), we did not use predetermined values: these were instead evaluated through the computer simulations using the temperatures obtained with thermal imaging following an optimization process.

The optimization process starts by setting a rational range of values in which k, α and R can vary. In the case of the thermal conductivity k, it is known that it can range between 2 and 2.5 W/m·K [23]. Similarly, the ranges for α and R were set according to values obtained experimentally as a function of wavelength in the range of 450–800 nm and for different processing times of the nc-YSZ [19]. For the samples used in our experiment, we consider that the absorption α decreases from 9000 m^{-1} for a wavelength of 600 nm, to 2400 m^{-1} for 800 nm. For the reflectivity R, this does not follow a marked tendency and the values vary between 11 and 17% for wavelengths of 450–800 nm; however, from 575 to 800 nm a continuous increasing tendency has also been observed [19]. Following these considerations, the tendencies and the speed at which these values change, we set for 810 nm a range of variation between 200 and 2400 m^{-1} for α, and a range between 10 and 20% for R. From these nominal values of α, the variation of this parameter as a function of temperature is considered in two ways: a linear or an exponential dependence with temperature (see Eqs. (4) and 5 in Appendix A). Table 1 shows the limit values of all the variables considered in the optimization problem; these were called *decision variables.* Meanwhile, the convection coefficients h_t and h_b did not show a significant influence on the obtained solutions, or at least they were not as influential as k, α or R. Nonetheless, we included h_t and h_b in the group of decision variables since we only know that they may vary between 2 and 25 (W/m^2·K) [25]. Thus, a rational range of values for these pa-

Table 1
Maximum and minimum values of the decision variables. k: thermal conductivity, R: reflection coefficient, α: absorption coefficient, h_t and h_b: thermal convection coefficients for top and bottom surfaces.

Variable	Minimum value (V_{min})	Maximum value (V_{max})	Refs.
k (W/m·K)	2	2.5	[23]
R (%)	10	20	[19]
α (m^{-1})	200	2400	[19]
h_t, h_b (W/m^2·K)	2	25	[25]

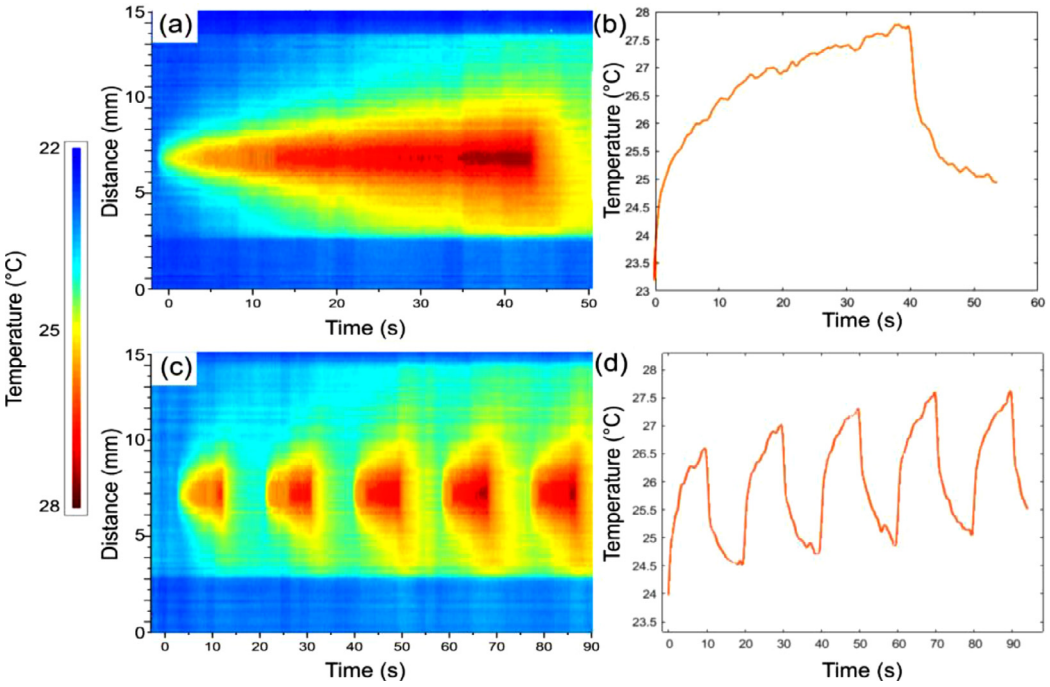

Fig. 4. Temperature variations as a function of time for two different irradiation sequences. The plots on the left show the laser irradiated regions obtained from thermal images and their temperatures as a function of time, while the plots on the right represent the maximum temperatures obtained from the images (central part of the spot registered by the thermal image).

rameters was obtained through this optimization technique, which is described in Appendix A.

4. Results

4.1. Experimental results

A typical sequence of thermal images obtained with this procedure is included in Fig. 2b showing the temperature changes registered when the laser was turned on and off. For each set of experiments, the temperature registered by the camera within the vicinity of the maximum temperature point was plotted as a function of time, yielding the plots included in Fig. 4. Clearly, the temperature increases when the laser is on while it decreases steadily once it is turned off. Notice also that the regions adjacent to the maximum temperature point also experience an increase in temperature (Fig. 4a and c). Using these data, we can further plot the maximum temperature as a function of time as shown in Fig. 4b and d. As seen in the plots of Fig. 4a and b, a 40 s time exposure yields a maximum temperature increase of approximately 2.8 °C, and the temperature drops steadily once the laser is turned off, returning to its initial value after approximately 7 s. In contrast, the plots shown in Fig. 4c and d depict the temperature variations registered for five consecutive sequences of 20 s each using a 50% duty cycle (i.e., 10 s laser on and 10 s laser off). It is evident from the thermal images that as the number of cycles increases, the maximum temperatures registered increase accordingly. Although the cooling time seems to allow for the sample to return to its initial temperature, it is evident from the figures that the temperature reaches higher values when the laser is on again. This is also observed in the plot showing the variations of the maximum temperature as a function of time (Fig. 4d); in this case, the maximum temperature increase was registered to be within 4.5 °C achieved after the fourth sequence of laser irradiation. This thermal imaging analysis shows that for the irradiation conditions used in our experiments, the temperature increase is well below 10 °C, hence remaining within acceptable limits to avoid tissue damage. This agrees with a previous report with an *in vitro* experiment [20].

4.2. Computer models results

The optimization process for computational model was based on calibrating the materials parameters (k, α and R) using the temperatures registered with the thermal camera. For each experiment (Experiment 1: 1 cycle, 40 s laser on, 15 laser off; and Experiment 2: 4 cycles of 10 s laser on and 10 s laser off, and 1 cycle of 10 s laser on and 5 s laser off), we compared the temperatures obtained at the center of the irradiated region, located in the origin of the coordinate system of the 2D axial geometry (see Fig. 3b). Fig. 5 shows the temperature evolution at this location obtained from the experiments and from the computational models after the optimization process. The figure further shows the influence of the variations in the absorption coefficient as a function of temperature (see Eqs. (4) and (5) in Appendix A for details); notice that the computational results match quite well the experimental measurements, regardless of the type of thermal variation considered for the absorption coefficient (i.e., linear or exponential dependence with temperature).

Further analysis of the agreement between the results from the experimental and the computer models is shown in Fig. 6. Clearly, there is a linear relationship between both results for the two considered cases (linear and exponential dependence of α with temperature), as confirmed by the fitting parameters included in the plot. For both cases, the slopes of the linear fittings are close to 1, while the intercept yields a value of 0.5, which is very small for the tested temperature range (23.2–28 °C). The plots also include other optimization parameters obtained with the fitting (OF, RE, R^2), showing further evidence of the match of the fitting model: the relative error was very low ($RE = 3.6\%$), the variance R^2 was close to 1 ($R^2 = 0.96$), and the objective function showed a very low value ($OF = 0.04$). All the fitting parameters showed almost identical values for the linear and the exponential dependence of α.

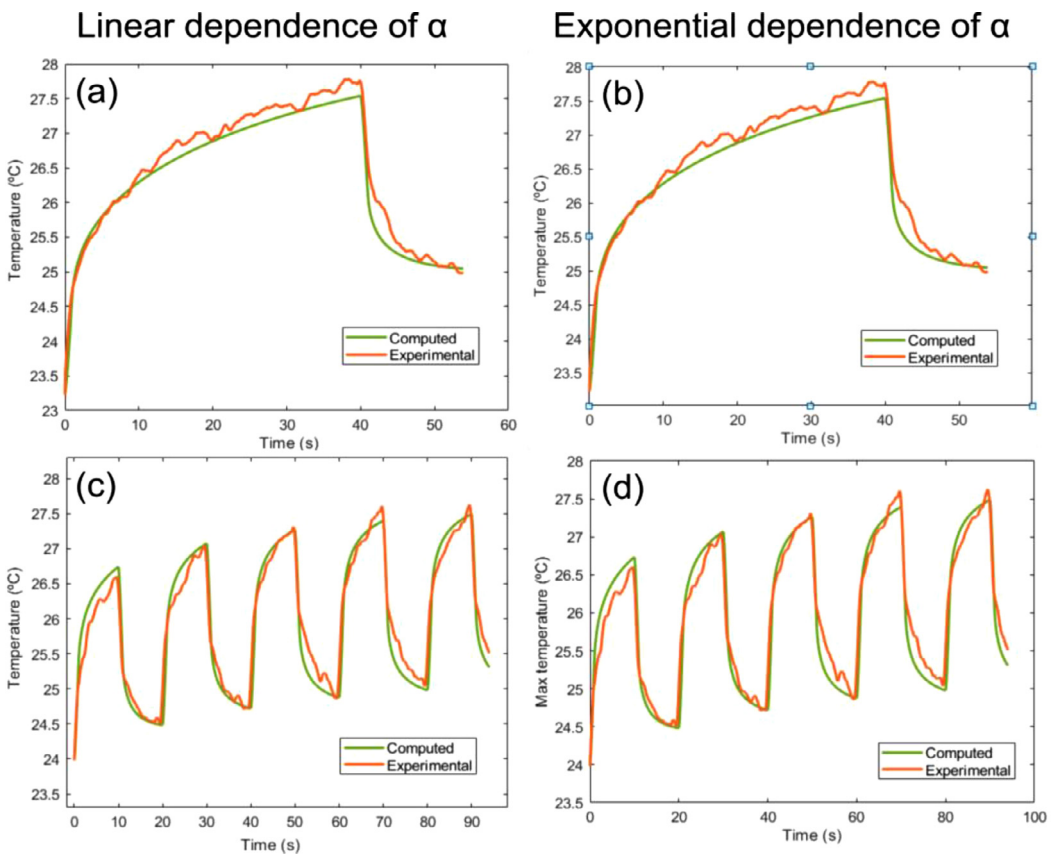

Fig. 5. Evolution of the maximum temperature in experimental and computational models for Experiment 1 (above) and Experiment 2 (below). The computed plots on the left were obtained considering a linear temperature variation in the absorption coefficient while the plots on the right consider an exponential variation as a function of temperature.

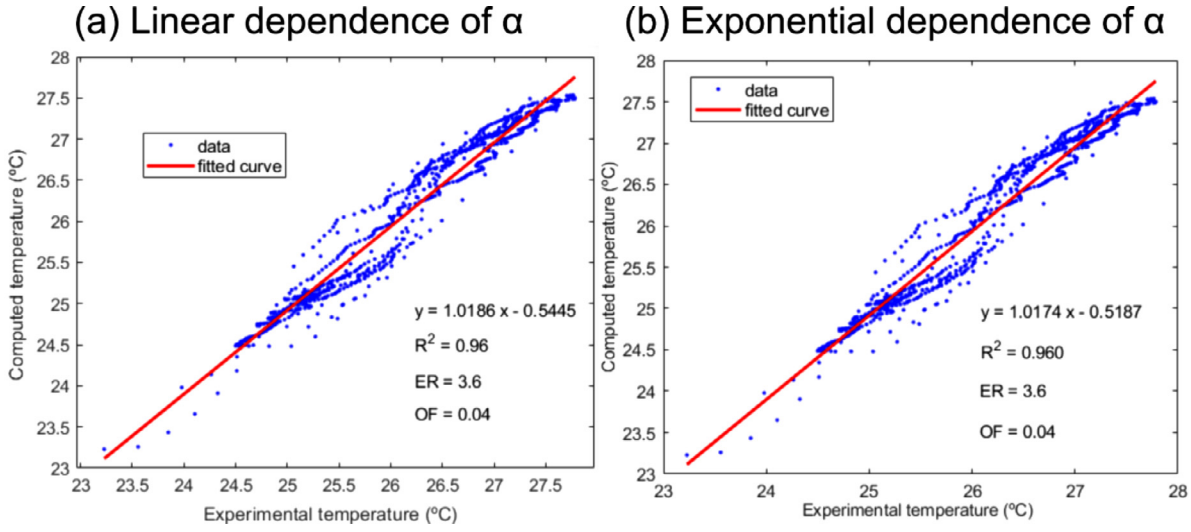

Fig. 6. Relationship between experimental and computational maximum temperatures and parameters of the fitting. On the left, computer results using a linear dependence of α with temperature; on the right, computer results using an exponential dependence.

With regard to the decision variables, their optimum values are shown in Table 2 for the two types of variations for the absorption coefficient (i.e., linear and exponential). The values for all decision variables did not change significantly, since the maximum difference was found to be 5.6% for the value for the absorption coefficient at the bottom. We can thus assume that these differences were negligible. To reinforce this, we notice that in Fig. 5a and b, the computer result are equal in both figures. If we overlap the green lines in Fig. 5a and b they will be coincident. The same observations can be made for Fig. 5c and d. The optimum value for the thermal conductivity was k = 2.13 and k =2.04 W/m·K, respectively, closer to the minimum value set for optimization (see Table 1). In contrast, the optimum value for the reflection coefficient (R=19% in both cases) was almost the same as that set for the maximum optimization value. For the absorption coefficient α we obtained $\alpha \in [426, 526]$ and $\alpha \in [433,502]$ for the linear and exponential relationships with temperature, respectively.

Table 2
Optimum values of the decision variables for the fit model assuming a linear and exponential relationship between T and α. *k: thermal conductivity* (W/m·K); *R: reflection* (%); α_0, α_1*: parameters of de linear and exponential dependence of* α; α*: absorption coefficient* (m^{-1}); h_t and h_b*: thermal convection coefficients* ($W/m^2 \cdot K$).

				Experiment 1		Experiment 2	
	k	R	α	h_t	h_b	h_t	h_b
Linear α dependence	2.13	19	[459,526]	16	16	11	11
Exponential α dependence	2.04	19	[433,502]	16	16	11	11

Table 3
Temperatures at the upper surface of the nc-YSZ from the experimental reported in [20] and from computer modeling.

	Experimental T (°C)	Computational T (°C)	Differences (%)
1 W	5.27	5.51	4.6
2 W	11,79	12.06	2.3
3 W	18.85	18.98	0.6
5 Hz, 3 W, 200 ms	16.55	17.20	3.9
1 Hz, 3 W, 400 ms	12.62	11.55	8.5
1 Hz, 3 W, 200 ms	8.93	8.08	9.8
0.5 Hz, 3 W, 200 ms	4.17	4.25	1.9
0.3 Hz, 3 W, 200 ms	2.06	2.10	1.9

Aside from comparing the computer and experimental results at the center of the laser beam (point of maximum temperatures, $r = 0$), we also compared the temperatures obtained in other points within the implant. Experimentally we obtained temperatures in the bottom surface of the implant, therefore we chose some points of this surface at different distances far from the center of the laser beam in arbitrary radial direction. Figs. 7 and 8 show the temperature evolution at the bottom surface of the implant for points located 0.5, 1, 1.5, 2, 2.5 and 3 mm away from the center of the laser beam (origin of the coordinates of the 2D axial geometry, see Fig. 3b) for Experiments 1 and 2. This figures were made using a linear α dependence, but the same results were obtained for exponential α dependence, as in the case of $r = 0$ (Fig. 5). For $r = 0$, the maximum difference between the experimental and computational results is 0.7%; however, larger differences of 4% can be observed in Figs. 7 and 8. Nonetheless, this larger difference is will within a reasonable value of 5%.

Finally, the computational model was used to reproduce the results reported in [20]. As shown Table 3, the computational results agree well with the reported temperatures. While the differences in temperature for continuous laser irradiation (1–3 W) are very small ($< 5\%$), in pulsed irradiation modes the resulting differences are higher only for the 1 Hz cases, although they remained below 10%.

5. Discussion

The results of the experimental setup described in Section 2 are used to assess the thermal behavior of the nc-YSZ samples. Specifically, our interest is to determine the temperature profile produced at the bottom of the sample surface. Our goal is to determine if the temperatures exceed the limit to produce thermal damage in tissue. In this sense, our results show that the temperature increase is below 10 °C, and consequently no tissue damage is expected under the laser irradiation conditions used in our experiments.

The experimental results were further used to calibrate the computational model replicating the thermal behavior of the nc-YSZ samples under different laser irradiation conditions. A direct comparison between the experimental and computational results show that this calibration procedure provides an effective means to obtain good predictions from the computational model. The quantitative results provide differences under a reasonable value of 5%, and qualitatively we observe a similar behavior of temperature evolution. The model was additionally used to reproduce the temperature values reported in [20] with similar conclusions. Differences in the temperatures are under a reasonable value of 5%, except for a specific case in which differences increases to an almost 10%.

Using the computational model we were able to obtain values for the parameters of the nc-YSZ sample that are involved in the generated photothermal effects. Through an optimization process, we obtained the values that better match the experimental results. These values were further used for reproducing the experimental results described in [20], yielding an excellent match and thereby validating the values for the thermal conductivity, absorption and reflectivity of the nc-YSZ obtained through the optimization process. These results were subsequently useful to assess the influence of these parameters (k, α and R) on the observed photothermal effects. After the fitting, results showed a great agreement between experimental and computer temperatures, with a maximum relative error of 3.6% found in the center of the laser in which the variance was $R^2 = 0.96$. From these results, it is clear that the absorption coefficient increases significantly with the temperature, but thus far we cannot deduce if this dependence is linear or exponential. In the linear relation, the absorption coefficient increased 14.54 m^{-1}/ °C, while for the exponential relation, the increase was temperature-dependent, varying between 14.03 to 15.84 m^{-1}/ °C for thee range of temperature considered in our experiments. Larger temperature ranges must be considered in order to analyze the absorption coefficient dependence with temperature. In addition, based on our results, we can state that this parameter is the most relevant for the photothermal effects observed in the nc-YSZ.

The use of the computational models can provide an effective means to evaluate the relevant thermal-optical parameters of nc-YSZ obtained with different manufacturing processes. Notice that these parameters may vary with the fabrication procedure, hence, the availability of a computational tool for predicting the photothermal effects of a given material is highly desirable. The procedure for obtaining the relevant information is simple and fast, and can be summarized in three steps: (1) obtain the temperature evolution in the bottom of upper surface of the nc-YSZ; (2) introduce this data in the computer model; and (3) assess the value of the

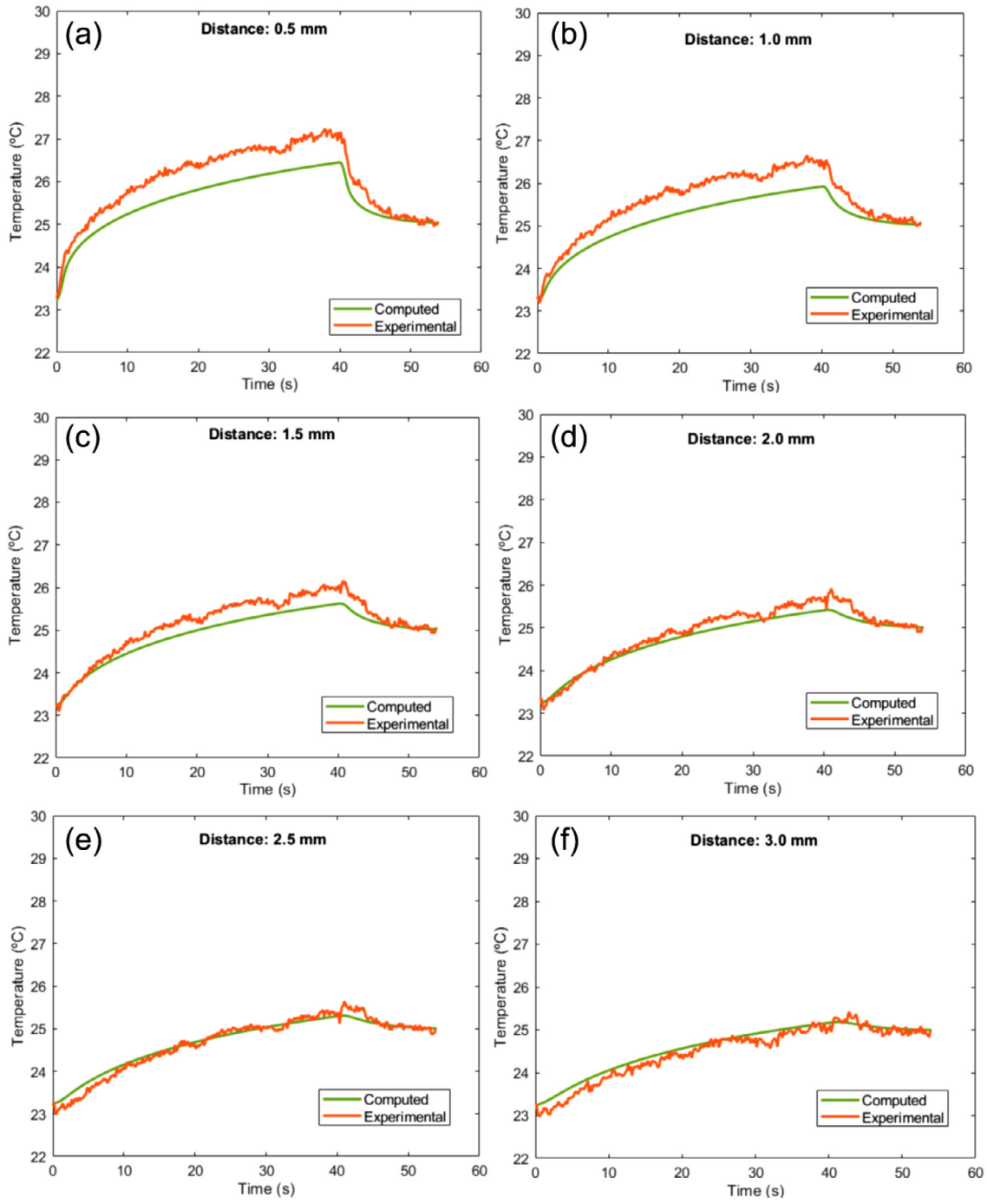

Fig. 7. Computed and experimental temperature evolution at different radial distances from the center of the laser beam for Experiment 1 using a linear α dependence.

parameters and fitting parameters. As seen from our results, the maximum differences were found in the center of the laser beam, therefore it is enough to establish the parameters using this location as the critical point for the fitting process.

An additional means that served for validating the computational model was simulation of the experimental conditions described in a previous report [20]. Our results matched closely those reported in these *in vitro* experiments, and we can therefore expect that the computational model may serve as a useful tool for predicting the temperatures that can be attained in the implant under different laser irradiation conditions. However, only temperatures at the upper surface of the implant are provided in [20], so the comparison is limited. Additional comparison with future experiments will reinforce the results and provide further data for improvements in the model. Clearly, the experimental conditions and the computational model used for this manuscript do not consider the conditions that the nc-YSZ would experience when used as a cranial implant. Such a scenario will require more elaborated experiments that will in turn lead to a computational model with increased complexity. Nonetheless, we expect that our results will set the grounds for future models that will allow to account for the thermal properties of the brain tissue and the relevant parameters involved in the generation of photothermal effects.

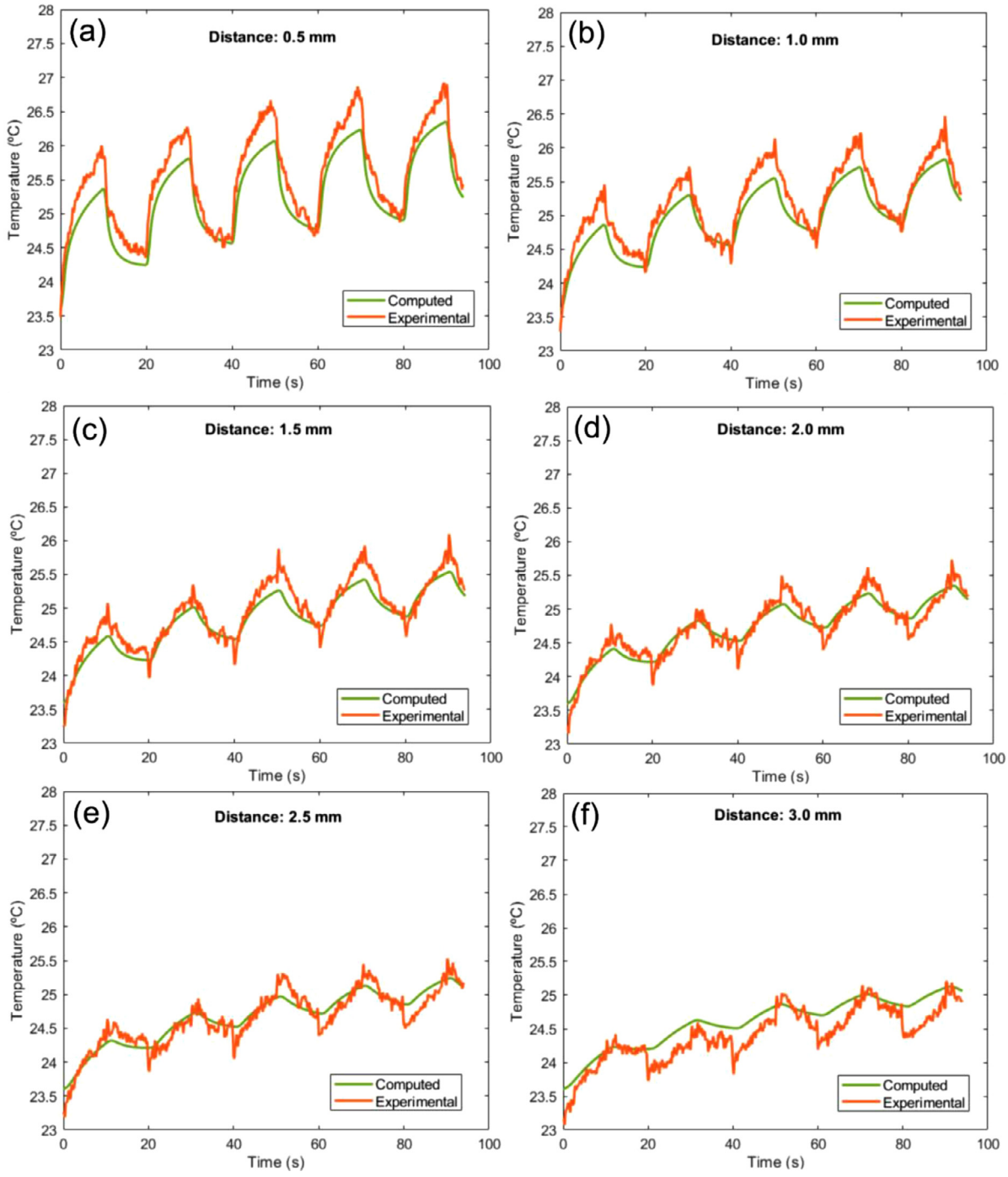

Fig. 8. Computed and experimental temperature evolution at different radial distances from the center of the laser beam for Experiment 2 using a linear α dependence.

6. Conclusions

Thermal imaging experiments reveal that thermal effects are readily generated in the nc-YSZ implant during the laser irradiation. The temperatures achieved for our experimental conditions are suitable for biomedical applications since they are always below temperature values that are known to produce thermal damage in biological tissue.

Using the results from thermal imaging experiments, we were able to calibrate a computational model describing the thermal effects generated in the implant under laser irradiation. This approach allowed us to estimate values for the thermal-optical parameters of the nc-YSZ in a more precise manner, and assess their influence on the observed thermal effects. Specifically, we can obtain values for the thermal conductivity k, the absorption α and the reflection coefficient R. According to our results, the absorption α is the most influential parameter on the thermal effects generated through laser irradiation of the nc-YSZ samples.

The combination of experimental and computational models allowed for obtaining a better insight of the photothermal effects produced in nc-YSZ samples irradiated by a laser source. This study is particularly useful to assess the temperatures that can be

achieved on any samples of these materials, which are commonly used as implants for different applications. Therefore, out results may provide an initial path for building a clinically oriented model that may incorporate other biophysical aspects related to this material and its effect in the adjacent tissues when irradiated by a laser.

Declaration of Competing Interest

The authors declare that they have no known competing financial interests or personal relationships that could have appeared to influence the work reported in this paper.

Funding and acknowledgments

This work was supported by the Spanish Ministerio de Ciencia, Innovación y Universidades under "Programa Estatal de I+D+I Orientada a los Retos de la Sociedad", Grant No. "RTI2018–094357-B-C21". The WttB project is being funded by NSF through grants NSF -PIRE 1545852, NSF -EAGER 1547014 and by CONACYT (México) through FORDECyT-PRONACES, Grant 246648. M.S.C.V. acknowledges support from "Beca Mixta, Grant 741249" (CONACYT, México).

Appendix A. Optimization

A.1. Subsidiary relationships

In addition to the range of values, α could depends on temperature. Therefore, we assumed two types of dependencies: linear (Eq. (4)) and exponential (Eq. (5))

$$\alpha = \alpha_0 + \alpha_1 T \tag{4}$$

$$\alpha = \alpha_0\, e^{-\frac{\alpha 1}{T}} \tag{5}$$

According to the maximum and minimum value of α set in Table 1, the range of variation of the parameters α_0 and α_1 was:

$$\alpha_0 \in [200 - \alpha_1 T_{min},\ 2400 - \alpha_1 T_{max}] \alpha_1 \in \left[0,\ \frac{2400 - 200}{T_{max} - T_{min}}\right]$$

$$\alpha_0 \in \left[200 e^{\frac{\alpha_1}{T_{max}}},\ 2400 e^{\frac{\alpha_1}{T_{min}}}\right] \alpha_1 \in \left[0,\ ln\left(\frac{25}{2}\right) \frac{1}{\frac{1}{T_{min}} - \frac{1}{T_{max}}}\right]$$

for the linear and exponential relationship, respectively. T_{min} and T_{max} were the minimum and maximum values of temperatures achieved in the point which registered the maximum experimental temperature. α_1 was the slope of the linear relationship defined in Eq. (4), which could be positive and negative. It was known that the value of the absorption coefficient increases with temperature, therefore, we considered that α_1 was positive and we made previous computations to verify it.

In the case of h_t and h_b the problem was to obtain a suitable value of the heat transfer coefficients [25] that took part in the heat transfer by natural convection between the implant (horizontal plate) and the air. In this sense, the values h_t and h_b were computed from

$$h_i = \frac{Nu_i k_a}{L} \tag{6}$$

where the subscript i refers to the bottom or top surface, k_a the thermal conductivity of air estimated from at film temperature, and L the characteristic dimension of the system calculated considering the surface area (A_S) and the perimeter (P) of the horizontal plate ($L = A_S/P$). Nu is the Nusselt number, whose value could vary from bottom to top surfaces, and it was computed using a theoretical develop found in [26–28].

A.2. Mathematical model fitting

The mathematical model was fitted to the experimental data to determine the values of the decision variables. With this aim, an optimization problem was formulated:

- Objective Function (OF). We compared the maximum temperatures at the bottom surface obtained from the experimental (Tm_{exp}) and computational (Tm_{com}) models. Therefore, the OF was average of the quadratic residues between these temperature difference.

$$OF = \frac{1}{N} \sum_{i=1}^{n} (Tm_{exp_i} - Tm_{com i})^2 \tag{7}$$

- Decision variables. To give the same importance to each decision variable, they were normalized. The normalized value V_N of each decision variable was calculated from its minimum and maximum values set in Table 1:

$$V_N = \frac{V - V_{min}}{V_{max} - V_{min}} \tag{8}$$

Therefore, the vector of the decision variables was

$$\overrightarrow{VD} = [k_N,\ \alpha_{0N},\ \alpha_{1N}\, R_N,\ h_{tN}, h_{bN}]$$

The average value of the relative error (RE) regarding the difference between experimental and computational temperatures, and the variance (R^2) were used to evaluate the accuracy of fit. The average value of the relative errors is a measure of the random component in the estimation and R^2 indicates the proportion of variance that is accounted for by the model. Additionally, a lineal fit between experimental and computed values was made. The parameters of the line ($y = ax + b$) and the R^2 of the fit give information about the model fitting goodness.

The experimental data obtained in Experiment 1 and 2 were together considered to have the largest amount of data and greater range of values available.

A.3. Computational tools

To solve the optimization problem, the *surrogateopt* function of Matlab R2019a (MathWorks, Natick MA, USA) was used. This Matlab function suited to OF that take a long time to evaluate, such as in the present case. The solver searches for the global minimum of a real-valued OF in multiple dimensions, subject to bound constraints.

To calculate the OF, it was necessary to solve the formulated mathematical model. For this purpose we used Comsol Multiphysics software (Comsol, Burlington MA, USA). PARDISO (parallel sparse direct solver) linear system solver and the BDF (backward differentiation formula) method of time stepping were used by Comsol to solve the mathematical model.

References

[1] S.F. Wang, J. Zhang, D.W. Luo, F. Gu, D.Y. Tang, Z.L. Dong, G.E. Tan, W.X. Que, T.S. Zhang, S. Li, L.B. Kong, Transparent ceramics: processing, materials and applications, Prog. Solid State Chem. 41 (1–2) (2013) 20–54, doi:10.1016/j.progsolidstchem.2012.12.002.

[2] O. Guillon, J. Gonzalez-Julian, B. Dargatz, T. Kessel, G. Schierning, J. Räthel, M. Herrmann, Field-assisted sintering technology/spark plasma sintering: mechanisms, materials, and technology developments, Adv. Eng. Mater. 16 (7) (2014) 830–849, doi:10.1002/adem.201300409.

[3] K. Nakamura, T. Kanno, P. Milleding, U. Örtengren, Zirconia as a dental implant abutment material: a systematic review, Int. J. Prosthodont. 23 (4) (2010) 299–309 PMID: 20617217.

[4] G.S. Kaliaraj, M. Bavanilathamuthiah, K. Kirubaharan, D. Ramachandran, T. Dharini, K. Viswanathan, V. Vishwakarma, Bio-inspired YSZ coated titanium by EB-PVD for biomedical applications, Surf. Coat. Technol. 307 (2016) 227–235, doi:10.1016/j.surfcoat.2016.08.039.
[5] P. Christel, A. Meunier, J.M. Dorlot, J.M. Crolet, J. Witvoet, L. Sedel, P. Boutin, Biomechanical compatibility and design of ceramic implants for orthopedic surgery, Ann. N. Y. Acad. Sci. 523 (1) (1988) 234–256, doi:10.1111/j.1749-6632.1988.tb38516.x.
[6] S.R. Casolco, J. Xu, J.E. Garay, Transparent/translucent polycrystalline nanostructured yttria stabilized zirconia with varying colors, Scr. Mater. 58 (6) (2008) 516–519, doi:10.1016/j.scriptamat.2007.11.014.
[7] Y. Xiong, Z. Fu, V. Pouchly, K. Maca, Z. Shen, Preparation of transparent 3 Y-TZP nanoceramics with no low-temperature degradation, J. Am. Ceram. Soc. 97 (5) (2014) 1402–1406, doi:10.1111/jace.12919.
[8] A. Rosenflanz, M. Frey, B. Endres, T. Anderson, E. Richards, C. Schardt, Bulk glasses and ultrahard nanoceramics based on alumina and rare-earth oxides, Nature 430 (7001) (2004) 761–764, doi:10.1038/nature02729.
[9] U. Anselmi-Tamburini, J.N. Woolman, Z.A. Munir, Transparent nanometric cubic and tetragonal zirconia obtained by high-pressure pulsed electric current sintering, Adv. Funct. Mater. 17 (6) (2007) 3267–3273, doi:10.1002/adfm.200600959.
[10] S. Grasso, B.N. Kim, C. Hu, G. Maizza, Y. Sakka, Highly transparent pure alumina fabricated by high-pressure spark plasma sintering, J. Am. Ceram. Soc. 93 (9) (2010) 2460–2462, doi:10.1111/j.1551-2916.2010.03811.x.
[11] J. Hernández-Cordero, R. Ramos-García, S. Camacho-López, G. Aguilar, A new window for photonics in the brain, IEEE Photonics Soc. Newsl. 32 (1) (2018) 4–8.
[12] Y. Damestani, C.L. Reynolds, J. Szu, M.S. Hsu, Y. Kodera, D.K. Binder, B.H. Park, J.E. Garay, M.P. Rao, G. Aguilar, Transparent nanocrystalline yttria-stabilized-zirconia calvarium prosthesis, Nanomed. Nanotechnol. Biol. Med. 9 (8) (2013) 1135–1138, doi:10.1016/j.nano.2013.08.002.
[13] M.S. Cano-Velázquez, N. Davoodzadeh, D. Halaney, C. Jonak, D.K. Binder, J. Hernández-Cordero, G. Aguilar, Enhanced near infrared optical access to the brain with a transparent cranial implant and scalp optical clearing, Biomed. Opt. Express 10 (7) (2019) 3369–3379, doi:10.1364/BOE.10.003369.
[14] N. Davoodzadeh, M.S. Cano-Velázquez, D.L. Halaney, C. Jonak, D.K. Binder, G. Aguilar, Evaluation of a transparent cranial implant as a permanent window for cerebral blood flow imaging, Biomed. Opt. Express 9 (10) (2018) 4879–4892, doi:10.1364/BOE.9.004879.
[15] N. Davoodzadeh, M.S. Cano-Velázquez, D.L. Halaney, C.R. Jonak, D.K. Binder, G. Aguilar, Optical access to arteriovenous cerebral microcirculation through a transparent cranial implant, Lasers Surg. Med. 51 (10) (2019) 920–932, doi:10.1002/lsm.23127.
[16] N. Davoodzadeh, M.S. Cano-Velázquez, D.L. Halaney, C.R. Jonak, D.K. Binder, G. Aguilar, Evaluation of a transparent cranial implant for multi-wavelength intrinsic optical signal imaging, in: Proceedings of the Neural Imaging and Sensing 2019, 10865, International Society for Optics and Photonics, 2019 108650B, doi:10.1117/12.2511035.
[17] D.L. Halaney, C.R. Jonak, J. Liu, N. Davoodzadeh, M.S. Cano-Velázquez, P. Ehtiyatkar, H. Park, D.K. Binder, G. Aguilar, Chronic brain imaging across a transparent nanocrystalline yttria-stabilized-zirconia cranial implant, Front. Bioeng. Biotechnol. 8 (2020) 659, doi:10.3389/fbioe.2020.00659.
[18] M.I. Gutierrez, E.H. Penilla, L. Leija, A. Vera, J.E. Garay, G. Aguilar, Novel cranial implants of yttria-stabilized zirconia as acoustic windows for ultrasonic brain therapy, Adv. Healthc. Mater. 6 (21) (2017) 1700214, doi:10.1002/adhm.201700214.
[19] J.E. Alaniz, F.G. Pérez-Gutierrez, G. Aguilar, J.E. Garay, Optical properties of transparent nanocrystalline yttria stabilized zirconia, Opt. Mater. 32 (1) (2009) 62–68, doi:10.1016/j.optmat.2009.06.004.
[20] Y. Damestani, N. De Howitt, D.L. Halaney, J.E. Garay, G. Aguilar, Evaluation of laser bacterial anti-fouling of transparent nanocrystalline yttria-stabilized-zirconia cranial implant, Lasers Surg. Med. 48 (8) (2016) 782–789, doi:10.1002/lsm.22558.
[21] I. Mellal, A. Oukaira, E. Kengene, A. Lakhssassi, Thermal therapy modalities for cancer treatment: a review and future perspectives, Int. J. Appl. Sci. 4 (2) (2017) 14, doi:10.21767/2394-9988.100064.
[22] W.L. Titsworth, G.J. Murad, B.L. Hoh, M. Rahman, Fighting fire with fire: the revival of thermotherapy for gliomas, Anticancer Res. 34 (2) (2014) 565–574 PMID: 24510985.
[23] S. Ghosh, D. Teweldebrhan, J.R. Morales, J.E. Garay, A.A. Balandin, Thermal properties of the optically transparent pore-free nanostructured yttria stabilized zirconia, J. Appl. Phys. 106 (2009) 113507, doi:10.1063/1.3264613.
[24] L.A. Dombrovsky, H.K. Tagne, D. Baillis, L. Gremillard, Near-infrared radiative properties of porous zirconia ceramics, Infrared Phys. Technol. 51 (1) (2007) 44–53, doi:10.1016/j.infrared.2006.11.003.
[25] A.H. Pelegrina, R.E. Echarte, G.H. Crapiste, Cálculo de las propiedades del aire húmedo y su aplicación en la simulación de procesos: VII taller de herramientas de cálculo en ingeniería de alimentos, Servicio de Publicaciones de la Universitat Politècnica de València, Santiago de Chile, 2001.
[26] R.H. Perry, D.W. Green, J.O. Maloney, Perry's, Chemical Engineers Handbook, 7th ed., McGraw-Hill, USA, 1997.
[27] G. Ruocco, Introduction to Transport Phenomena Modeling. A Multiphysics, General Equation-Based Approach, Springer, Gewerbestrasse, 2018.
[28] W.H. McAdams, Heat Transmission, McGraw-Hill, New York, 1954.